

Article

Time-Resolved Corrosion Behavior of Transition-Metal-Based High-Entropy Alloy in Saline and Phosphate Buffer Solutions

Baran Sarac 

Erich Schmid Institute of Materials Science, Austrian Academy of Sciences, 8700 Leoben, Austria;
baran.sarac@oeaw.ac.at

Abstract: This study focuses on time-resolved surface modifications of a single-phase $\text{Ti}_{25}\text{Zr}_{25}\text{Nb}_{15}\text{V}_{15}\text{Ta}_{20}$ high-entropy alloy (HEA) when immersed in 0.9 wt% NaCl and phosphate-buffer solutions (PBS) at 37 °C. A remarkable transition from high ionic diffusion to electron conduction was observed in PBS, whereas the existing conductivity in NaCl solution was further enhanced after 3 h of exposure. During in-situ testing, NaCl improved passivation conceived by the decrease in passivation-current density and increase in Tafel slope. Heterogeneously dispersed oxide particles with NaCl could have accounted for the moderate increase in conductivity while not affecting the capacitive behavior. The Tafel slope decreased after 2 h of immersion in PBS linked to K^+ and P^{-3} accumulation on the surface. The pronounced change in the post-PBS treated sample was also revealed by a four-fold increase in HEA-electrolyte resistance. A visible decrease in the constant-phase-element parameter of the HEA-electrolyte interface after long-term PBS immersion indicated a rise in electrode conductivity and ionic build-up on the surface. The findings suggest that compared to PBS, the selected HEA has a faster passive-layer formation in NaCl with smaller changes in interface resistivity upon long-term immersion, which is promising for enhanced protein-adsorption rates and loading amount.

Keywords: high-entropy alloy; transition metal; biocorrosion; electrochemical-impedance spectroscopy; potentiodynamic polarization; energy-dispersive X-ray



Citation: Sarac, B. Time-Resolved Corrosion Behavior of Transition-Metal-Based High-Entropy Alloy in Saline and Phosphate Buffer Solutions. *Metals* **2023**, *13*, 951.
<https://doi.org/10.3390/met13050951>

Academic Editor: Branimir N. Grgur

Received: 19 March 2023

Revised: 5 May 2023

Accepted: 11 May 2023

Published: 14 May 2023



Copyright: © 2023 by the author. Licensee MDPI, Basel, Switzerland. This article is an open access article distributed under the terms and conditions of the Creative Commons Attribution (CC BY) license (<https://creativecommons.org/licenses/by/4.0/>).

1. Introduction

High-entropy alloys (HEAs), discovered by Yeh et al. and Cantor et al. in 2004 [1,2], are a unique class of alloys with favorable thermal, magnetic, hydrogen-storage, mechanical, and biomedical properties [3–11]. HEAs contain five or more main elements, each within 5 to 35 wt% in equi-/near-equi-molar concentrations [12,13]. During their synthesis, four core effects, namely, (1) high configurational entropy stabilizing the solid solutions relative to intermetallic phases, (2) severely strained lattices bestowing different effects on mechanical and physical properties, (3) sluggish diffusion kinetics because of the fluctuations in the bonding environment, and (4) a “cocktail effect” generated by inter-element interactions yielding composite structures and outstanding properties, are utilized [13]. HEA fibers with excellent performance potential are desired for functional, structural, and biomedical applications [14–16].

E-beam melting has clear advantages over other conventional methods since it enables production of refractory and chemically active materials with the crucible-free melting mode [17–19], resulting in microfibers with close tolerances and high quality. This crucible-free melting method yields micro/nanocrystalline or amorphous structures with a single phase due to rapid ($\sim 10^6 \text{ K}\cdot\text{s}^{-1}$) quenching rates [18].

Different HEAs have been hitherto studied in terms of electrocatalytic activity, passivity and passivation behavior, diffusion kinetics, and electron-transfer reactions in aqueous solutions [20–27]. However, the samples were either in bulk, ribbon, or nanocatalyst forms. Our recent publication [28] focuses on the electrochemical-corrosion behavior and hydrogen activity of transition-metal-based HEA microfibers composed of IVB (Ti, Zr, Hf) and

VB (V, Nb, Ta) elements in 1 M KOH solution using potentiodynamic polarization, Tafel fitting, and the Butler–Volmer equation. The main findings indicated ultra-low corrosion down to several microns per year and a stable supercapacitive response over a wide range of frequencies originating from the oxide-layer formation. The highest stability with a very slight shift of the corrosion potential $\Delta E_{\text{corr}} = 5$ mV (from -451 mV to -446 mV) was observed for the $\text{Ti}_{25}\text{Zr}_{25}\text{Nb}_{15}\text{V}_{15}\text{Ta}_{20}$ HEA, as the onset potential of the potentiodynamic polarization from a cathodic to an anodic regime iteratively increased at each cycle. Furthermore, the highest E_{corr} was attained for this alloy composition, which is indicative of better corrosion resistance.

It is possible that the stainless steel commonly used for surgical instruments, i.e., scalpels, forceps, operating tables, etc., is at risk of an accumulation of harmful bacteria, biofilm formation, and corrosion [29]. The high stability of the selected transition-group elements and their alloys in various environments can be beneficial for using HEA microfibers in saline solution for dentistry and simulated physiological solutions for surgeries and body implantations [30,31]. Along with their very high flexibility and strength [32,33], these HEA microfibers can be an alternative material for surgical tools.

In terms of HEAs, cast, cold-rolled, and annealed $\text{Fe}_{50}\text{Mn}_{27}\text{Ni}_{10}\text{Cr}_{13}$ [34]; CoCrFeMnNi fabricated by selective laser melting [35]; and laser-clad $\text{FeCoNiCrNb}_{0.5}\text{Mo}_x$ coatings [36] were reported to show acceptable corrosion performance in NaCl solution. However, until now, no studies besides that of our group have demonstrated the influence of corrosion on microfibers when they are in metallic form. This study concentrates on the time-dependent biocorrosion of the same HEA produced by electron-beam melting with a pendant-drop-melt extraction in saline and phosphate-buffer solutions at a standard body temperature of 37°C . The near-atomic $\text{Ti}_{25}\text{Zr}_{25}\text{Nb}_{15}\text{V}_{15}\text{Ta}_{20}$ HEA is preferred to its equiatomic counterpart, i.e., $\text{Ti}_{20}\text{Zr}_{20}\text{Nb}_{20}\text{V}_{20}\text{Ta}_{20}$, because TiZr alloys have been shown many times to achieve excellent osseointegration and biocompatibility [37–40]. Furthermore, it was recently reported that the inclusion of Ta in Ti-Zr leads to ZrO_2 and Ta_2O_5 formation and to improved corrosion resistance compared to cp-Ti and Ti-6Al-4V alloys [41]. For these reasons, we increased the amount of Ti and Zr while retaining Ta. Our initial trial of this composition in 0.9 wt% NaCl at room temperature yielded promising results (Figure 6 in [28]). In the current study, frequency-dependent alterations as a function of immersion time were examined by electrochemical impedance spectroscopy (EIS) and simulated by a suitable equivalent-circuit model (ECM) to extract the resistive and capacitive behavior of the bulk sample and the formed oxide layer. The stability of the samples over immersion time was tested by potentiodynamic polarization, where the linear Tafel slopes determined the changes in the cathodic activity. The single-phase structure of the as-spun fibers was confirmed by X-ray diffraction (XRD) and scanning-electron-microscopy (SEM) imaging, whereas surface modifications due to oxide accumulation were registered by energy-dispersive X-ray (EDX) attached to SEM.

2. Materials and Methods

2.1. HEA-Microfiber Synthesis

Granules of Zr (99.5%), Ti (99.5%), V (99.7%), Nb (99.95%), Hf (99.5%), and Ta (99.95%) were used for the preparation of ingots by arc-melting (Edmund Bühler GmbH). The microfibers were produced by a custom-built device in which electron-beam melting of the billet in a vacuum chamber takes place. In this technique, the lower end of a vertical billet melts with the formation of a hanging melt drop. Billets in the form of rods with cm-sized diameters are used. The drop solidifies once it contacts the rotating isosceles triangle and detaches from the tip of the ingot due to centrifugal forces. High cooling rates of up to $10^6\text{ K}\cdot\text{s}^{-1}$ can be possible, allowing for a nanocrystalline or amorphous structure depending on the composition. Discrete fibers with sizes of components smaller than those of traditional spraying can be achieved using this method [18]. The compositional homogeneity of the microfibers was previously verified by cross-sectional high-angle annular dark-field-scanning transmission electron microscopy (HAADF-STEM) and elemental mapping with

energy-dispersive X-ray [28]. The microfibers were rectangular in cross-section and had an average width of $235 \pm 15 \mu\text{m}$, a thickness of $15.3 \pm 1 \mu\text{m}$, and a length of $2 \pm 0.2 \text{ cm}$.

2.2. Electrochemical Measurements

A premixed aqueous phosphate-buffer solution (PBS) (ROTI®Cell PBS— Na_2HPO_4 : 5.599 mM, KH_2PO_4 : 1.058 mM, NaCl: 154.004 mM, pH = 7.4 ± 0.1 , Carl Roth GmbH + Co. KG) and a 0.9 wt% NaCl aqueous solution (CELLPURE® $\geq 99.5\%$, Carl Roth GmbH + Co. KG) were prepared for this study. In order to reduce the corrosion rates and increase the polarization resistance of the stainless steel, a 5 mL solution with electrodes at very close distances was deaerated for the measurements for 15 min using Ar gas. Since the microfiber area was extremely small, a metal wrap between the clamp and microfiber was utilized in order to hold the material tight and straight and establish conductivity during electrochemical measurements. One microfiber edge was coiled by copper tape (Busch 1799) to fit into clips (SKS Hirschmann KLEPS 2600), which mediated high electrical conductivity. Before the test, the microfiber–Cu-tape junction was proven to be electrically conductive by a multimeter, where the electrical conductivity of the Cu tape was measured to be $65 \text{ MS}\cdot\text{m}^{-1}$, yielding an extremely small resistivity of $0.0154 \mu\Omega\cdot\text{m}$. The samples were immersed in the solution preheated to $37 \pm 1^\circ\text{C}$ in a conventional cell using a hot plate with a temperature probe, and measurements were conducted immediately after reaching the temperature. During the measurements, the cell was covered by Parafilm® in order to eliminate oxygen entrance and exit and minimize the change in solution concentration. The electrochemical measurements were conducted using a Pt-counter electrode 0.8 mm in diameter and an Ag(s)/AgCl(s) reference electrode in a saturated KCl solution. The redox potential of the Ag/AgCl electrode in the test solutions can be estimated by the following: The redox potential of PBS is $+0.640 \text{ V}$ ($E_{\text{Ag}/\text{AgCl}} + E^\circ_{\text{Ag}/\text{AgCl}} (0.197 - 0.00101 \times T (37-25)) \text{ V} + 0.0615 \times \text{pH} (7.4)$) vs. a reference hydrogen electrode (RHE). For 0.9 wt% NaCl, this value is $+0.523 \text{ V}$ ($E_{\text{Ag}/\text{AgCl}} + E^\circ_{\text{Ag}/\text{AgCl}} (0.197 - 0.00101 \times T (37-25)) \text{ V} + 0.0615 \times \text{pH} (5.5)$) vs. RHE. The immersed surface areas were $0.030 \pm 0.006 \text{ cm}^2$ within NaCl and $0.029 \pm 0.002 \text{ cm}^2$ within PBS. Three samples in each solution were measured. The error margins due to surface roughness (vein-like patterns and striations stemming from the production) were determined by recording the optical micrographs with Olympus BX51 Fluorescence Microscope using the Olympus Stream Motion 1.9.3. software and analyzing with Gwyddion SPM data-visualization and -analysis software. Because of the selected microfiber-production technique, the deviation between the surface areas varied only slightly. An extremely sensitive PARSTAT 4000A Potentiostat Galvanostat (AMETEK GmbH, Meerbusch, Germany, equipped with a VersaStudio 2.62.2 software module) with an applied-voltage resolution of $30 \mu\text{V}$ for $\pm 1 \text{ V}$ signal and an applied-current accuracy of 0.2% of the reading was used for the measurements. The electrochemical measurements were performed using electrochemical-impedance spectroscopy (EIS) and a potentiodynamic polarization sweep (from cathode to anode) every 30 min of immersion time after EIS. It is important to note that the immersion time indicated in this paper is the total waiting time between measurements excluding the duration of EIS and polarization tests. The solution concentrations remained stable, confirmed by the pH meter before the electrochemical test and after the test was completed. In the beginning, EIS analysis was carried out at open-circuit potential (OCP) at 10 mV AC amplitude with 10 points per decade registered from 100,000 Hz to 0.1 Hz. OCP in 0.9 wt% NaCl and PBS solutions were recorded as 0.375 V and 0.025 V, respectively. The OCP analysis was measured for one minute before each EIS every 0.5 h, and the time-resolved OCP value stayed quite constant with each solution (within $\pm 5 \text{ mV}$). Equivalent-circuit modeling (ECM) of the EIS data was performed using the ZSimpWin V.3.10 analysis program. Potentiodynamic polarization was registered from $\pm 1 \text{ V}$ vs. OCP in 0.9 wt% NaCl and in PBS at a scan rate of $0.005 \text{ V}\cdot\text{s}^{-1}$. The overpotential was calculated by adding the shift of the actual potential from the equilibrium state (i.e., $+0.523 \text{ V}$ for 0.9 wt% NaCl and $+0.640 \text{ V}$ for PBS).

2.3. Determination of Crystalline State

Structural characterization of the HEA microfibers was performed using a Rigaku SmartLab 5-axis X-ray diffractometer with Co K α radiation ($\lambda = 1.7902 \text{ \AA}$) and Bragg–Brentano θ -2 θ configuration. The stack of HEA microfibers was glued to a (100) Si wafer by paraffin, and the scan was performed between 20° and 120° at a step size of 0.02°.

2.4. Morphology and Composition Investigation

The microstructural characterization of the microfiber samples was carried out by scanning electron microscopy between 500 \times (FoV: 558 μm) and 5000 \times (FoV: 55.8 μm) using TESCAN MAGNA with ultra-high resolution and high-contrast imaging equipped with a QUANTAX EDS for composition analysis. An acceleration voltage (AV) of 20 keV, an aperture size of 30 μm , and a working distance (WD) of 6 mm were employed for the scanning-electron-microscopy (SEM) imaging. Energy-dispersive-X-ray (EDX) analysis was performed at 5000 \times magnification with an AV of 20 keV and a WD of 8.5 mm, and at 3500 \times magnification with an AV of 20 keV and a WD of 8.6 mm for samples tested in NaCl and PBS solutions, respectively.

3. Results and Discussion

3.1. Morphology and Structural Analysis of As-Quenched Fiber

The morphological investigation of a rapidly quenched fiber showed a solidified river-like pattern formed during sputtering with some tiny pores. The pore size range determined from scanning electron microscopy was 0.5–6 μm (Figure 1b). The edge part of the fiber showed an irregular surface originating from the production conditions (Figure 1c). The XRD plot of the HEA indicated mainly a single-phase BCC structure (Figure 1d). The lattice parameter was calculated as $0.334 \pm 0.01 \text{ nm}$. The BCC structure was also corroborated previously by selected-area electron diffraction performed using transmission electron microscopy. In addition, the cross-sectional investigation by HAADF-STEM analysis corroborated the defect-free structure with high compositional homogeneity [28].

3.2. Electrochemical Impedance of HEA Microfibers

In order to evaluate the behavior of a $\text{Ti}_{25}\text{Zr}_{25}\text{Nb}_{15}\text{V}_{15}\text{Ta}_{20}$ HEA in simulated biological fluids, a procedure combining electrochemical-impedance spectroscopy followed by potentiodynamic polarization tests was performed immediately after immersion. These alternating tests were conducted at 30 min intervals for 3 h of immersion time. Before each EIS, 1 min of OCP determination was applied. Figure 2 depicts the Nyquist and Bode plots obtained in 0.9 wt% NaCl solution at 37 °C. The Nyquist plots showed, in all cases, a single semicircle characteristic of near-ideal charge-transfer resistance. The diameter of the incomplete semicircle tended to decrease for 30 min of immersion and then increase to the initial stage after 1 h (Figure 2a). This phenomenon could have been due to the unstable solution and electrode conditions right after immersion, which can take time to reach stability for different electrode–electrolyte systems [42]. However, one of the key investigation points of this paper is to analyze the in-situ changes while reaching stability. After this point, the semicircle diameter tended to decrease, indicating a continuous reduction in the resistance of this film, and hence, the Bode magnitude measured at the lowest frequency (0.1 Hz) decreased from $|Z| = \sim 46400$ to $\sim 34000 \text{ }\Omega\cdot\text{cm}^2$ (Figure 2b). In contrast, $|Z|$ at the highest measured frequency (100 kHz) directly measured from the plots was slightly higher after 3 h of immersion (c.f. ~ 2.7 for 1 h vs. $\sim 3.1 \text{ }\Omega\cdot\text{cm}^2$ for 3 h immersion). This change indicates that the electrode's kinetics in the selected solution and conditions varied oppositely in near-DC and high-frequency regions, where this transition could be observed in the 2–25 Hz range. This is also the region where the largest difference between the phase angles' φ was observed ($\Delta\varphi = 6.6^\circ$ at 25 Hz) (Figure 2c). At 0.5 h, the maximum recorded φ was 81.1° at 316 Hz, whereas this point at 3 h shifted to 631 Hz with a slight drop in φ (79.7°). These findings show that the characteristic kinetics of the HEA in the low-, medium-, and high-frequency ranges varied remarkably upon immersion time.

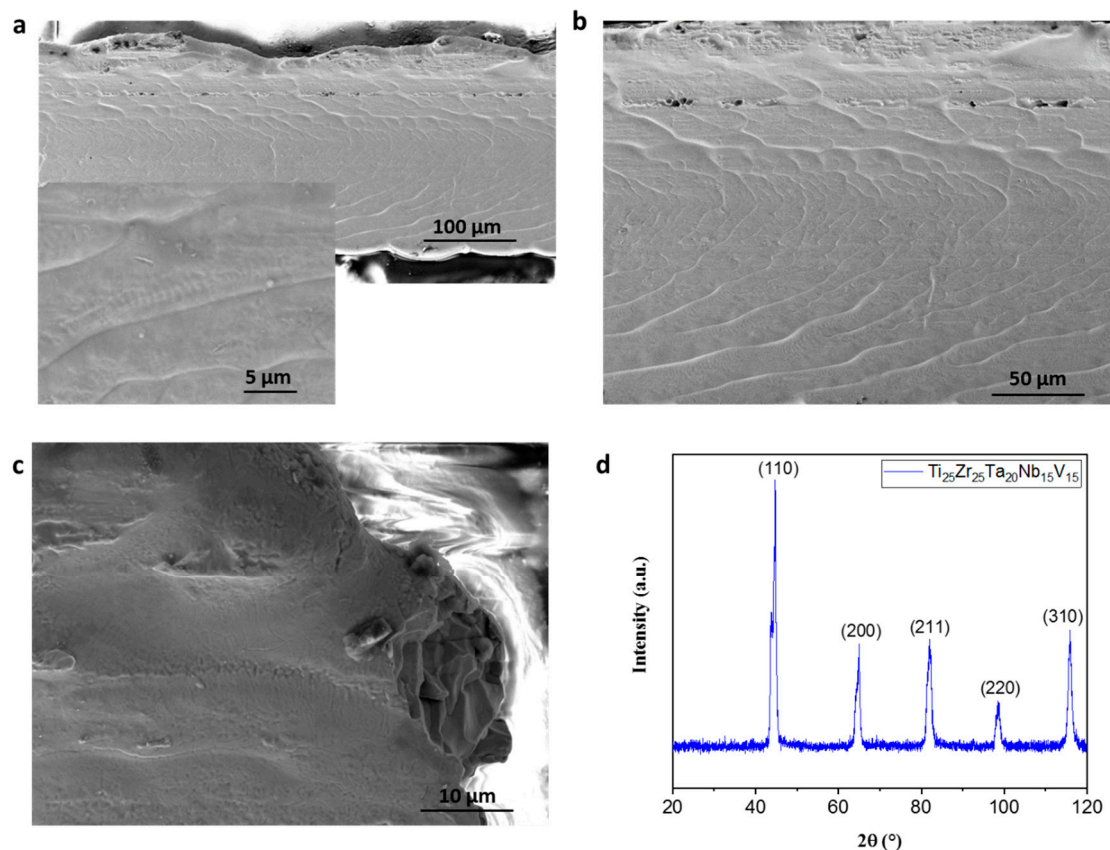


Figure 1. SEM imaging of a $\text{Ti}_{25}\text{Zr}_{25}\text{Nb}_{15}\text{V}_{15}\text{Ta}_{20}$ as-quenched fiber taken at (a-top) 1000 \times , (b) 2000 \times , and (c) 5000 \times . (d) The X-ray diffractogram of the single-BCC-phase HEA. (a-bottom) depicts the surface marks recorded at 10,000 \times .

When the same immersion protocol was applied in PBS solution at 37 °C, a transition from a capacitive (represented by a straight line) to conductive (represented by a semicircle—near-ideal charge-transfer resistance) circuit was observed within 3 h of immersion (Figure 3a). This change can be linked to the oxide-film formation as a barrier layer upon potentiodynamic polarization cycles, proven for a Ti–35.5Nb–7.3Zr–5.7Ta alloy tested under similar conditions [42]. HEA was unstable right after immersion, showing a relatively larger $|Z|$ values but reaching stability after 0.5 h immersion (cf. $6 \Omega \cdot \text{cm}^2$ for 0 h vs. $1.3 \Omega \cdot \text{cm}^2$ for 3 h immersion) (Figure 3b). After reaching stability, the maximum φ of 77° was observed at 1000 Hz (Figure 3c). The dramatic change in the Bode-phase profiles is related to double-layer formation mainly caused by the P^{-3} and K^{+} ions. Furthermore, compared to the NaCl solution, two-time constants at ~15 and ~1000 Hz were clearly visualized in this solution. Thus, compared to the 0.9 wt% NaCl solution at 37 °C, the changes in the electrode kinetics were more pronounced in the PBS solution at 37 °C upon long-term immersion.

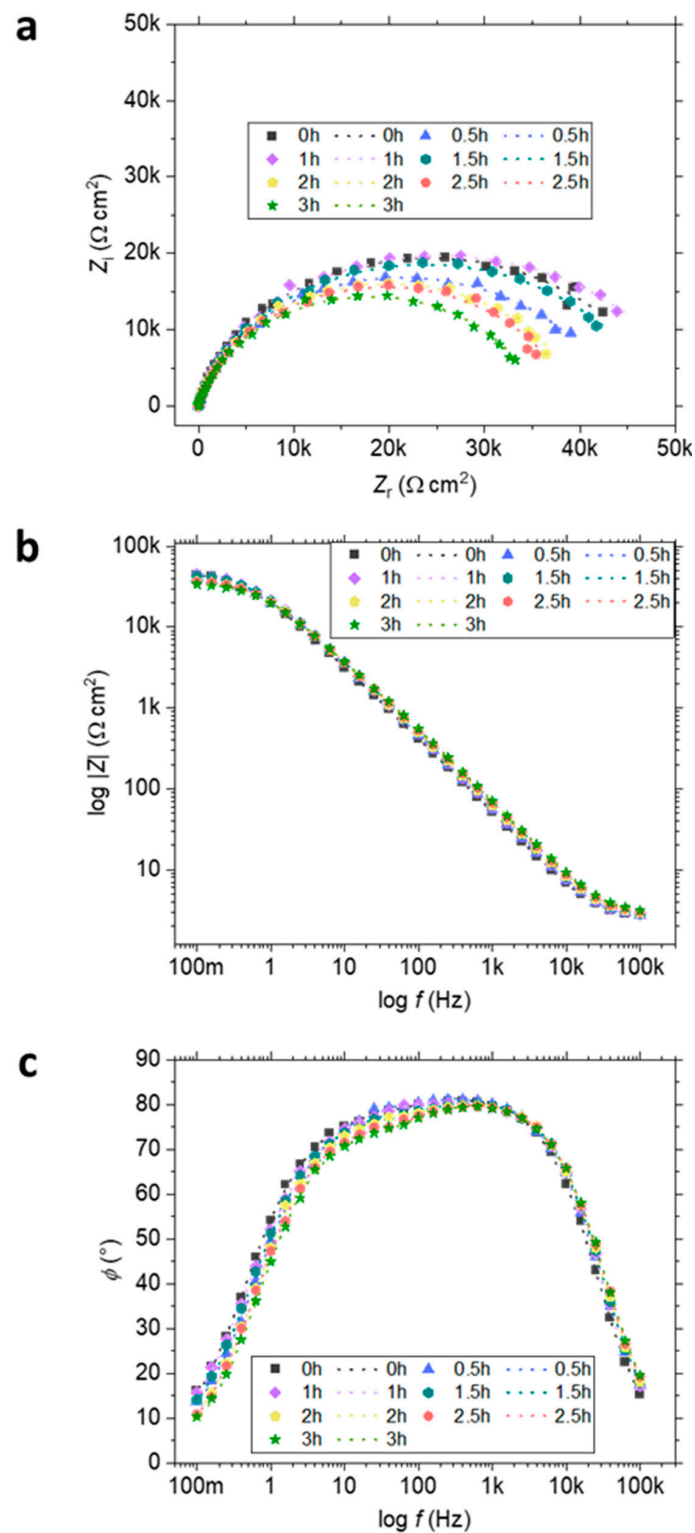


Figure 2. (a) Nyquist, (b) Bode-magnitude, and (c) Bode-phase plots of the $\text{Ti}_{25}\text{Zr}_{25}\text{Nb}_{15}\text{V}_{15}\text{Ta}_{20}$ HEA in 0.9 wt% NaCl solution at 37 °C. Measurements (scattered data) were taken at 30 min intervals and recorded at open-circuit potentials. The dotted lines indicate the simulated data using an $R(Q(R(QR)))$ equivalent-circuit model.

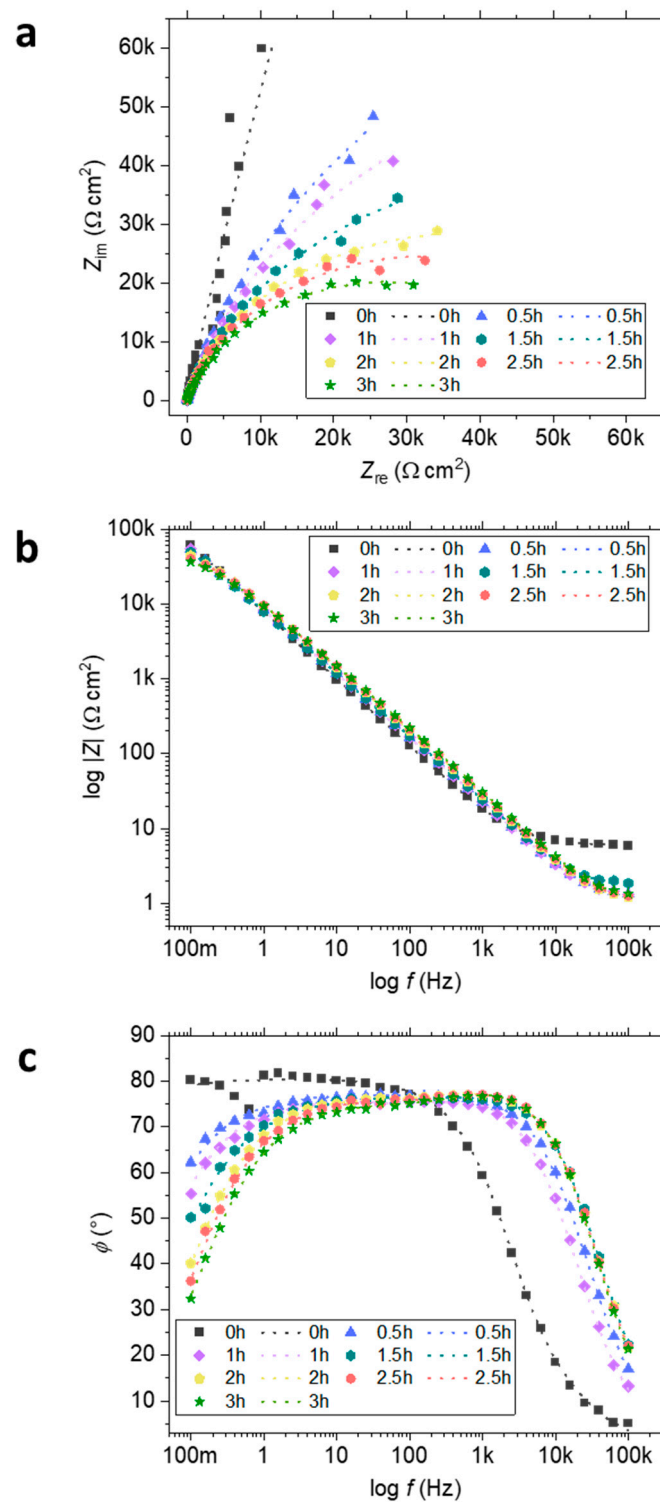


Figure 3. (a) Nyquist, (b) Bode-magnitude, and (c) Bode-phase plots of the $\text{Ti}_{25}\text{Zr}_{25}\text{Nb}_{15}\text{V}_{15}\text{Ta}_{20}$ HEA in PBS solution at 37 °C. Measurements (scattered data) were taken at 30 min intervals and recorded at open-circuit potentials. The dotted lines indicate the simulated data using an $R(Q(R(QR)))$ equivalent-circuit model.

3.3. Equivalent-Circuit Modeling

Table 1 and 2 show the simulation of the EIS data recorded at OCP performed in 0.9 wt% NaCl and PBS solutions at 37 °C, respectively. The EIS data were fitted by the following circuit model given in Tables 1 and 2. Here, Q_1 is the constant-phase element of

the double layer, and Q_2 is the constant-phase element of the native oxide and oxide–metal interface. Before the electrochemical measurements, a non-porous Zr-rich native oxide for this composition formed upon production was recorded as 1.5 nm by high-resolution transmission electron microscopy (see Figure S1 in [28]). The impedance of the constant-phase element had a direct relationship with Y and n , i.e., $Z(Q) = Y_0^{-1}(j\omega)^{-n}$, where $j = \sqrt{-1}$ and $\omega = 2\pi f$ [42]. Among all the circuit models, the $R(Q(R(QR)))$ model yielded the lowest chi-squared values ($\chi^2 < 10^{-4}$) for both the PBS and NaCl solutions. Our group has used similar types of circuits multiple times to indicate the influence of oxide on the hydrogen–metal interactions, methanol oxidation, and corrosion properties of different alloy types [43–45]. The two-time constants observed for both the NaCl and PBS solutions are represented by the electron transfer from the surface into the bulk state (represented by R_1 and Q_1) and the interaction between the oxide and double layer (represented by R_2 and Q_2). For the NaCl solution, the solution resistance R_s was minimal and almost constant after 3 h of immersion, indicating the electrolyte-sample stability from the beginning of the experiment. The constant-phase-element (CPE) parameter defining the double-layer capacitance Y_1 dropped from 5.9×10^{-6} to 4.7×10^{-6} S sⁿ cm⁻², which was probably linked to the time delay in establishing a stable electrode–electrolyte interface. During this time, an order-of-magnitude decrease in the charge-transfer resistance R_1 was observed (from ~4900 to ~460 Ω cm²). After this point, a rise in R_1 values can refer to the oxide-layer growth as a function of immersion time. The high and stable CPE exponent n_1 values (>0.9) followed a typical power law and indicated a relatively smooth surface [46]. The CPE parameter for the oxide and HEA–oxide interface Y_2 fluctuated as the immersion time increased, whereas the related resistance R_2 tended to decrease significantly (from 5300 to 3180 Ω ·cm²) between 1 and 3 h of immersion. This difference should mainly be related to the transition from a relatively rough surface to a relatively smoother one, as evidenced by the increase in the n_2 CPE exponent [46]. For the sample submerged in PBS, it is evident from EIS data that 0.5 h of immersion was necessary to bring the sample to stability. After this point, R_s became almost constant. Y_1 tended to decrease steadily from 1.8×10^{-6} to 1.1×10^{-6} as 3 h of immersion was reached. On the other hand, no clear correlation can be made with the R_1 , which seemed to decrease at 1.5 h and increase again. The high n_1 values refer again to the smooth surface. A four-fold drop in R_2 (HEA–electrolyte resistance, from ~220,000 to ~55,500) and the increase in Y_2 (CPE parameter of HEA–electrolyte interface) indicate a rise in the electrode conductivity due to the possible ionic build-up on the surface. On the other hand, the roughness factor related to n_2 did not play a major role in these changes.

Table 1. ECM of the Ti₂₅Zr₂₅Nb₁₅V₁₅Ta₂₀ HEA in 0.9 wt% NaCl solution at 37 °C using the $R(Q(R(QR)))$ model. Very high fitting reliability ($\chi^2 < 10^{-4}$) is present for all measurements.

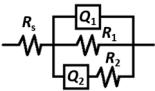
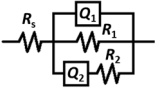
	0 h	0.5 h	1 h	1.5 h	2 h	2.5 h	3 h
R_s (Ω cm ²)	2.492	2.428	2.559	2.611	2.593	2.666	2.744
Y_1 (S s ⁿ cm ⁻²)	5.893×10^{-6}	5.503×10^{-6}	4.699×10^{-6}	4.692×10^{-6}	4.905×10^{-6}	4.749×10^{-6}	4.722×10^{-6}
n_1 (–)	0.9265	0.9248	0.9324	0.9287	0.923	0.92	0.9166
R_1 (Ω cm ²)	3917	4908	459.4	1568	2802	3574	4104
Y_2 (S s ⁿ cm ⁻²)	3.84×10^{-6}	4.52×10^{-6}	4.293×10^{-6}	4.043×10^{-6}	3.427×10^{-6}	3.722×10^{-6}	3.65×10^{-6}
n_2 (–)	0.6632	0.5633	0.6157	0.6603	0.7085	0.7378	0.7606
R_2 (Ω cm ²)	4.577×10^4	4.032×10^4	5.31×10^4	4.74×10^4	3.77×10^4	3.583×10^4	3.183×10^4
χ^2	3.233×10^{-4}	1.990×10^{-4}	2.045×10^{-4}	1.640×10^{-4}	1.631×10^{-4}	1.706×10^{-4}	1.386×10^{-4}

Table 2. ECM of the $\text{Ti}_{25}\text{Zr}_{25}\text{Nb}_{15}\text{V}_{15}\text{Ta}_{20}$ HEA in PBS solution at 37 °C using the R(Q(R(QR))) model. Very high fitting reliability ($\chi^2 < 10^{-4}$) is present for all measurements except 0 h.

	0 h	0.5 h	1 h	1.5 h	2 h	2.5 h	3 h
R_s ($\Omega \text{ cm}^2$)	5.911	1.182	1.705	0.9315	1.032	1.08	1.16
Y_1 ($\Omega \text{ cm}^{-2}$)	1.241×10^{-5}	1.803×10^{-5}	1.694×10^{-5}	1.343×10^{-5}	1.285×10^{-5}	1.186×10^{-5}	1.109×10^{-5}
n_1 (–)	0.9191	0.8908	0.8913	0.9066	0.9047	0.9083	0.9103
R_1 ($\Omega \text{ cm}^2$)	5.463	527.5	650.6	192	505.5	448.4	448
Y_2 ($\Omega \text{ cm}^{-2}$)	1.231×10^{-5}	7.444×10^{-6}	9.671×10^{-6}	1.219×10^{-5}	9.644×10^{-6}	1.06×10^{-5}	1.201×10^{-5}
n_2 (–)	0.867	0.7067	0.7175	0.692	0.6997	0.6974	0.6949
R_2 ($\Omega \text{ cm}^2$)	2.73×10^6	2.198×10^5	1.57×10^5	1.106×10^5	7.655×10^4	6.69×10^4	5.558×10^4
χ^2	1.335×10^{-3}	3.088×10^{-4}	4.396×10^{-4}	2.491×10^{-4}	1.597×10^{-4}	5.840×10^{-4}	1.774×10^{-4}

3.4. Time-Resolved Potentiodynamic Polarization

The potentiodynamic polarization curves within NaCl at 37 °C as a function of immersion time showed relatively smooth and repeatable behavior, particularly in the cathodic regime (Figure 4a). Even though the corrosion potential stayed at almost a constant value of $E_{\text{corr}} = 0.270 \pm 0.015$ V, the corrosion current density J_{corr} tended to decrease from 3.4×10^{-6} A cm $^{-2}$ to 1.6×10^{-6} A cm $^{-2}$. J_{pass} values were determined from the last point of the straight part of the anodic section, where the deviation point from straightness was confirmed by intersecting with a straight line. The passivation current J_{pass} steadily dropped from 7.3×10^{-6} A cm $^{-2}$ to 2.2×10^{-6} A cm $^{-2}$. The main goal was to examine a time-resolved study of the electrodes due to ion accumulation on the surface and not by building up a new oxide layer. For this reason, the potentiodynamic polarization curves were stopped at early stages (i.e., right after observing the passivation-current density). These findings confirm that although the corrosion resistance decreased upon immersion time, a better passivity in a wide range was observed. A peak at 0.130 V was pronounced after long-term immersion, which can be linked to metastable pitting. Conversely, the potentiodynamic polarization taken in the PBS solution at 37 °C showed a very high scatter in the short-term immersion but tended to become relatively smoother as the immersion time increased (Figure 4b). Here, it must be noted that the PBS data were smoothed by a 10-point sliding-average function to show the transition in terms of immersion time. The smoothing was necessary, particularly for the zero and first hours of testing. This may be because the ionic balance was established at later stages in the PBS solution. E_{corr} tended to shift towards positive values (from -0.214 V to -0.146 V) as the immersion time increased. In the meantime, the passivation current increased to $J_{\text{pass}} = 9.2 \times 10^{-6}$ A cm $^{-2}$. J_{pass} resembled the commercially pure Ti and Ti-4Al-6V (~ 1 – 10 $\mu\text{A cm}^2$) tested under similar conditions [47]. During this 3 h immersion time, the corrosion resistance increased for the PBS solution to 4.0×10^{-6} A cm $^{-2}$. The evolution of the electrochemical parameters as a function of time is summarized in Table 3. The general finding is that the J_{corr} and J_{pass} decreased for the NaCl and increased for the PBS solutions after 3 h.

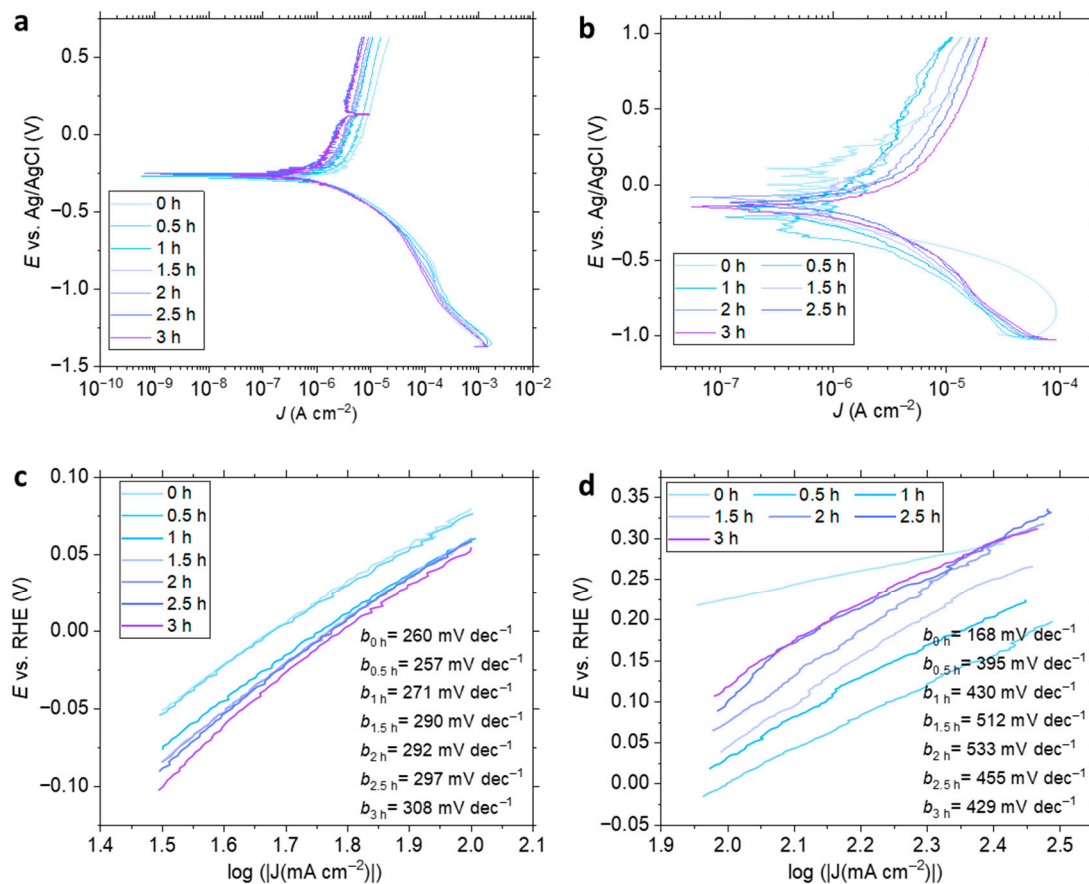


Figure 4. Potentiodynamic polarization of the Ti₂₅Zr₂₅Nb₁₅V₁₅Ta₂₀ HEA in (a) 0.9 wt% NaCl and (b) PBS solutions at 37 °C. (c,d) Corresponding Tafel plots.

Table 3. Comparison of the potentiodynamic polarization tests of Ti₂₅Zr₂₅Nb₁₅V₁₅Ta₂₀ HEA in 0.9 wt% NaCl and PBS solutions at the initial stage (0 h) and every 0.5 h of immersion time until 3 h. E_{corr} and J_{corr} were determined by the extrapolation of the cathodic and anodic branches and intersecting them with the steady-state OCP as described in [48]. Note that N/A corresponds to values that cannot be accurately measured.

Solution—Time	E_{corr} (mV)	J_{corr} (A cm ⁻²)	J_{pass} (A cm ⁻²)
NaCl—0 h	-292 ± 2	$3.4 \pm 0.2 \times 10^{-6}$	$7.3 \pm 0.4 \times 10^{-6}$
NaCl—0.5 h	-272 ± 2	$3.4 \pm 0.3 \times 10^{-6}$	$5.9 \pm 0.2 \times 10^{-6}$
NaCl—1 h	-268 ± 2	$2.4 \pm 0.1 \times 10^{-6}$	$4.0 \pm 0.2 \times 10^{-6}$
NaCl—1.5 h	-266 ± 6	$2.2 \pm 0.1 \times 10^{-6}$	$3.8 \pm 0.2 \times 10^{-6}$
NaCl—2 h	-258 ± 4	$2.2 \pm 0.1 \times 10^{-6}$	$3.4 \pm 0.2 \times 10^{-6}$
NaCl—2.5 h	-255 ± 2	$1.6 \pm 0.1 \times 10^{-6}$	$2.5 \pm 0.1 \times 10^{-6}$
NaCl—3 h	-260 ± 5	$1.6 \pm 0.1 \times 10^{-6}$	$2.2 \pm 0.1 \times 10^{-6}$
PBS—0 h	N/A	N/A	N/A
PBS—0.5 h	-214 ± 2	N/A	N/A
PBS—1 h	-142 ± 2	N/A	N/A
PBS—1.5 h	-148 ± 2	$1.9 \pm 0.1 \times 10^{-6}$	$5.5 \pm 0.1 \times 10^{-6}$
PBS—2 h	-82 ± 2	$3.3 \pm 0.3 \times 10^{-6}$	$6.8 \pm 0.2 \times 10^{-6}$
PBS—2.5 h	-118 ± 4	$3.7 \pm 0.3 \times 10^{-6}$	$7.9 \pm 0.2 \times 10^{-6}$
PBS—3 h	-146 ± 2	$4.0 \pm 0.3 \times 10^{-6}$	$9.2 \pm 0.3 \times 10^{-6}$

In comparison to cp-Ti, although J_{corr} was several times larger for the selected HEA, in this study, E_{corr} was significantly more positive, cf. ~ -527 mV vs. ~ -260 mV vs. Ag/AgCl (value after the stabilization of the OCP) in 0.9 wt% NaCl solution at 37 °C [49]. TiZr (Nb, Hf,

Ta) medium-entropy alloys (MEAs) exhibited J_{corr} on the nA cm^{-2} levels in 0.9 wt% NaCl, which was mainly because the samples were in bulk form (on mm scale) and had a remarkably smaller surface-area-to-volume ratio, and experiments were conducted at room temperature. Nevertheless, in the same paper, it is reported that these MEAs showed more negative E_{corr} (between -380 mV and -490 mV vs. Ag/AgCl) [50], indicating a higher probability of occurrence of corrosion [51]. The measured J_{corr} values were in the same order of magnitude with FeCoNiCrNb_{0.5}Mo_x HEA with a relatively more positive E_{corr} [52]. J_{corr} and/or E_{corr} values retrieved in this study were smaller than those of most of the other HEAs, including CoCrFeNi(Cu) [53], FeCrCoAlMn_{0.5}Mo_{0.1} [54], (CoFe₂NiV_{0.5}Mo_{0.2})_{100-x}Nb_x [55], CoCrFeNi(W_{1-x}Mo_x) [56], CoCrFeNiTi_x [57], AlCoCrFeNiTi_x [58], and 316L [54] stainless steel in the literature at various NaCl concentrations and temperatures.

In the PBS solution, although the Ti-Zr-Nb MEAs exhibited lower J_{corr} values, Ti₂₅Zr₂₅Nb₁₅V₁₅Ta₂₀ HEA showed a more positive E_{corr} (<-148 mV after stabilization) in comparison to E_{corr} , ranging from -400 mV to -600 mV vs. SCE for the MEA alloys [59]. E_{corr} of the TiZrHfNbFe_x ($x = 0, 0.25, 0.5, 0.75, 1, 1.5$, and 2) was also slightly more negative in the PBS solution, with relatively better corrosion resistance, which may be because the experiments were conducted at room temperature with slower ion activity [60]. In bulk form, Ti₂₀Zr₂₀Nb₂₀Ta₂₀Mo₂₀ HEA showed $E_{\text{corr}} = -607 \pm 55$ mV vs. SCE in PBS at 37°C [30]. Furthermore, the present HEA showed superior corrosion resistance compared to 316L stainless steel at 37°C in PBS [61].

The Tafel slope for the NaCl solution increased from 260 to 308 $\text{mV}\cdot\text{dec}^{-1}$, which could be linked to the ionic balance reached after 1.5 h as well the surface ions, i.e., Cl^- . (Figure 4c). Interestingly, for the PBS solution, the Tafel slope started to show a rapid decrease (from 533 to 429 $\text{mV}\cdot\text{dec}^{-1}$) after 2 h of immersion (Figure 4d). This was also when the potentiodynamic polarization curves became smoother, and sharp V-shape profiles can be observed in Figure 4b. This finding may be related to the K^+ and P^{-3} ions, as discussed later in the energy-dispersive-X-ray analysis.

McCafferty reported on the corrosion activity of conventional iron in various deaerated electrolytes at different temperatures [48]. The example given for the 0.6 M NaCl solution (equal to 0.9 wt% NaCl) at room temperature had a steep anodic slope and horizontal cathodic-extrapolation line. On the other hand, the selected high-entropy alloy, in our case, showed a very symmetric polarization profile for the curves where J_{corr} could be determined (see Table 3). Figure S1a and S1b show the polarization curves and extrapolation from cathodic and anodic branches and their intersection at OCP for representative scans in 0.9 wt% NaCl at 1 h and in PBS at 1.5 h, respectively. The cathodic and anodic branch extrapolated back intersected at the steady-state OCP potential, which means that both branches were under activation control, corrosion happened uniformly, changes in electrode potential did not induce additional electrode reactions, and there were well-defined Tafel regions present on these dashed lines [48]. This method also confirmed the validity of the cathodic Tafel slopes presented in Figure 4c,d.

3.5. Post-Electrochemical-Composition Analysis

Figure 5a shows a representative SEM micrograph of an HEA after 3 h of NaCl immersion. Figure 5b–k represents the EDX elemental mapping of the sample after NaCl immersion. The homogenous distribution of Ti (Figure 5b), Zr (Figure 5c), Nb (Figure 5d), V (Figure 5e), and Ta (Figure 5f) was confirmed for the overall sample. The phase contrast in the middle part of Figure 5a was Na, Cl, and O rich (Figure 5g–i), as can be visualized from the superimposed EDX analysis in Figure 5j. In comparison, the superimposed EDX analysis of the as-cast sample (Figure 5k) showed a homogenous elemental distribution across the sample without any accumulation from the solvents or oxide formation due to electrochemical-corrosion tests. Based on the results and literature, the OH^- , O^{2-} , and Cl^- ions from the electrolyte were expected to be adsorbed on the surface by interacting with metallic surfaces assessed by first-principle calculations [62].

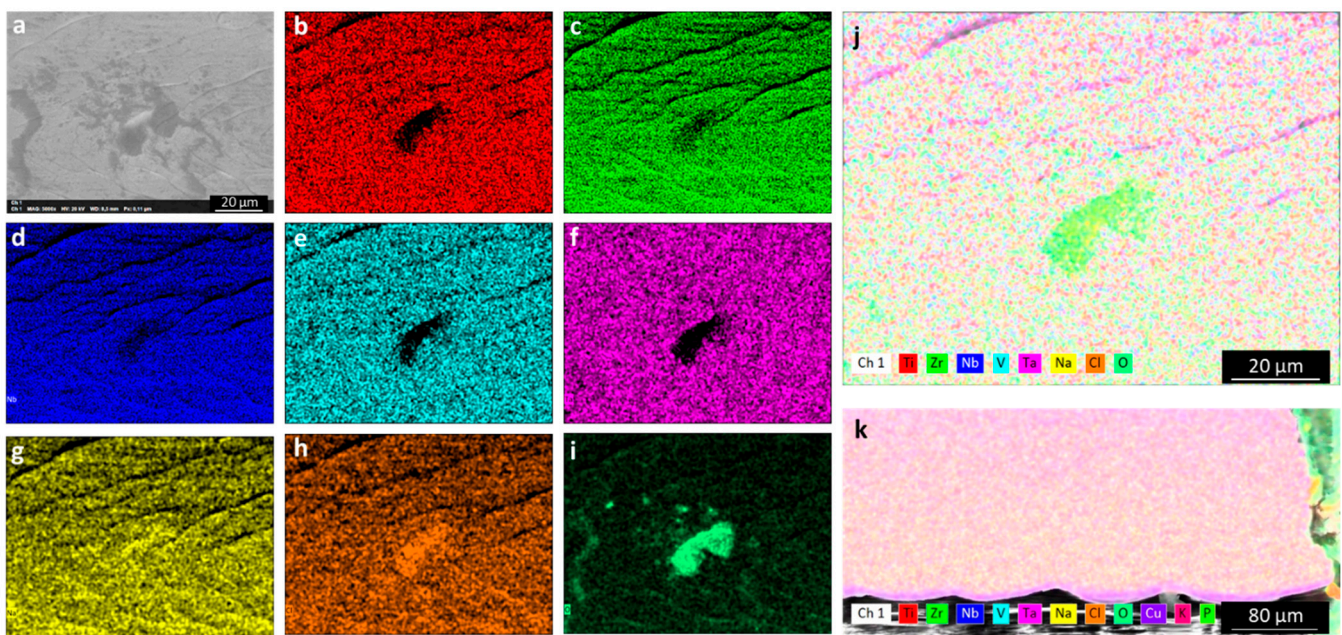


Figure 5. (a) SEM micrographs of the $\text{Ti}_{25}\text{Zr}_{25}\text{Nb}_{15}\text{V}_{15}\text{Ta}_{20}$ HEA submerged in 0.9 wt% NaCl at 37 °C. Corresponding EDX elemental mapping for (b) Ti, (c) Zr, (d) Nb, (e) V, (f) Ta, (g) Na, (h) Cl, and (i) O. (j) The superimposed EDX image including all the investigated elements. (k) Comparative superimposed EDX image of the as-spun sample.

After submerging the sample for 3 h in PBS solution, the SEM micrograph showed a phase contrast (Figure 6a). Figure 6b–l represents the EDX elemental mapping of the sample after PBS immersion. The superimposed EDX analysis showed yellowish spots (Figure 6b). There was no remarkable change in the elements of the HEA (Figure 6b–g). There was homogenous P (Figure 6h) and K (Figure 6i) absorbance on the surface of the PBS solution, where potassium was relatively more concentrated in some regions on the top and bottom sections of the microfiber. Strong localization for the Na, Cl, and partial oxygen indicates oxide-particle accumulation in the presence of salt. The X-ray-fluorescence analysis previously confirmed the existence of phosphate groups bound to the surface [63].

A new oxide-layer formation after electrochemical tests should not be expected since neither NaCl and PBS nor water (with a very small amount of dissolved $\text{OH}^- = 10^{-7} \text{ mol}\cdot\text{L}^{-1}$ [64]) can provide sufficient OH^- ions that can build up a new oxide layer. SEM observations before and after electrochemical measurements in NaCl and PBS solutions in this study as well as in KOH and H_2SO_4 solutions in our previous study [28], revealed that the regions of ion accumulation are independent of the pore locations that come from casting. In general, for the sample submerged in NaCl, the oxide, sodium, and chloride particles were recorded. For the samples submerged in PBS, in addition to oxide, phosphorus and potassium accumulation was present. Since the potentiodynamic polarization scans were stopped in the anodic region right after passivation, the samples did not show any pits or cracks after potentiodynamic polarization. Another important finding is that samples rinsed with distilled water after electrochemical tests did not exhibit any K, P, Na, Cl, or O segregation, resulting in an EDX map similar to that in Figure 1k (see Figure S2). Hence, it can be deduced that the particle accumulation happened after measurement upon drying and not by a surface reaction between HEA and the mentioned elements.

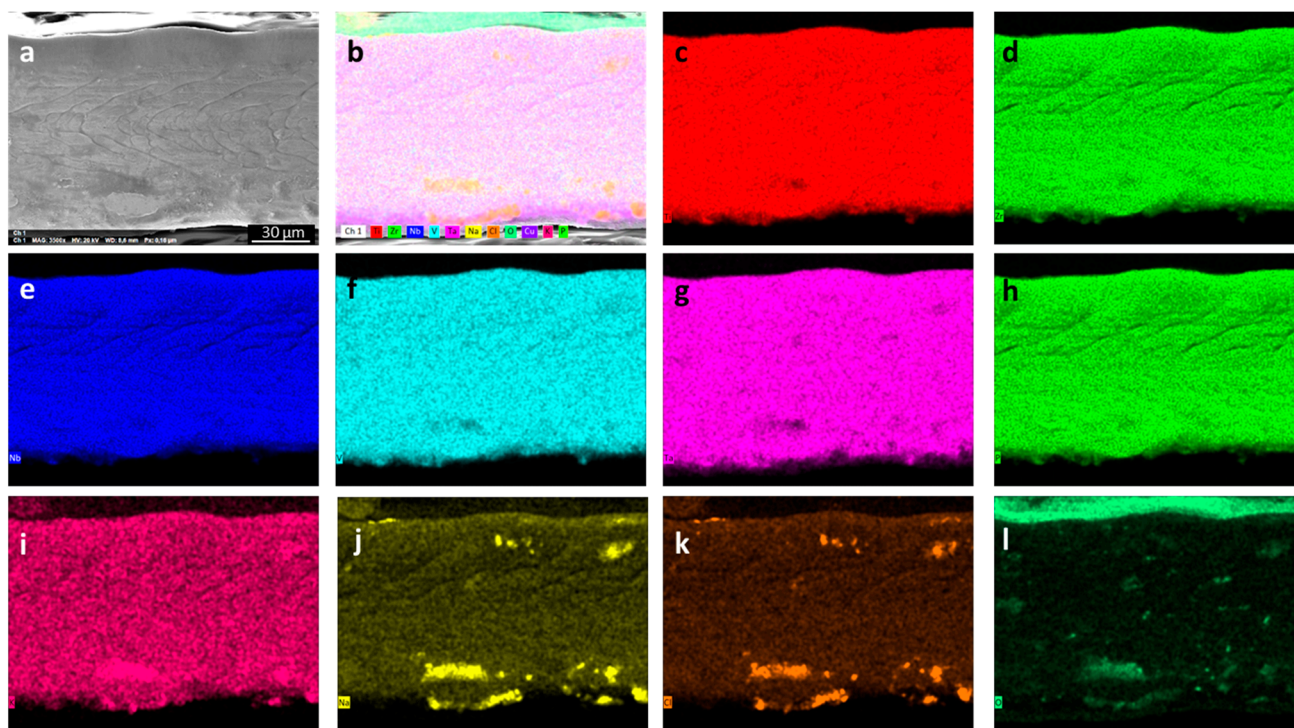


Figure 6. (a) SEM micrographs of the $\text{Ti}_{25}\text{Zr}_{25}\text{Nb}_{15}\text{V}_{15}\text{Ta}_{20}$ HEA submerged in PBS solution at 37 °C. (b) The superimposed EDX image including all the investigated elements. Corresponding EDX microanalysis for (c) Ti, (d) Zr, (e) Nb, (f) V, (g) Ta, (h) P, (i) K, (j) Na, (k) Cl, and (l) O.

4. Conclusions

This study examined the time-dependent electrochemical behavior of $\text{Ti}_{25}\text{Zr}_{25}\text{Nb}_{15}\text{V}_{15}\text{Ta}_{20}$ HEA microfibers and the modifications in the surface morphology and chemistry in 0.9 wt% NaCl and standard PBS solutions at 37 °C. The potentiodynamic polarization results in the NaCl solution showed high stability along with of an increase in corrosion resistance. Resistance decreased as immersion time increased, reflected by an increase in the Tafel slope from 260 to 308 $\text{mV} \cdot \text{dec}^{-1}$. The potentiodynamic polarization curves of the HEA sample within the PBS solution became relatively smoother as the immersion time increased, confirming that the time to reach stability within the PBS solution was longer than that of the NaCl solution. The Tafel slope started to decrease after 2 h of immersion, probably because of the K^+ and P^{-3} accumulation of the surface originating from the PBS solution. Despite the very high surface area per volume compared to bulk samples and coatings, the corrosion-current-density values were moderately low, with extremely low corrosion potentials in both 0.9 wt% NaCl and PBS solutions at 37 °C. An extensive transition from a capacitive to a conductive electrode was observed within 3 h of immersion in PBS, whereas this difference was much less in NaCl, and the size of the semicircle became slightly smaller, indicating a continuous reduction in the resistance of the oxide film. Compared to NaCl, with only some decrease in resistivity values (by ~30%) of R_2 (HEA-electrolyte resistance), the 50-fold drop in R_2 within 3 h of immersion and the increase in Y_2 (CPE parameter of HEA-electrolyte interface) after 2 h of PBS immersion indicated an increase in electrode conductivity and ionic buildup on the surface.

Supplementary Materials: The following supporting information can be downloaded at: <https://www.mdpi.com/article/10.3390/met13050951/s1>. Figure S1: Extrapolated cathodic and anodic branches and their intersection with the steady-state OCP potential at 37 °C for (a) 0.9 wt% NaCl at 1 h and (b) PBS solutions at 1.5 h, Figure S2: Sample surface after polarization in PBS solution and subsequent rinsing with water.

Funding: This research received no external funding.

Institutional Review Board Statement: Not applicable.

Informed Consent Statement: Not applicable.

Data Availability Statement: The raw/processed data required to reproduce these findings cannot be shared at this time as the data are related to an ongoing study.

Acknowledgments: The investigation part of this work is supported by The Austrian Science Fund (FWF) under project grant I3937-N36. The author thanks Mikhail Serov for the synthesis and procurement of the microfibers. The author thanks Eray Yüce for his assistance with SEM and EDX measurements and Amir Rezvan for his assistance with XRD measurement. The author also thanks Vladislav Zadorozhnyy, A. Sezai Sarac, and Tolga Karazehir for the fruitful discussions on electrochemical corrosion and microfiber production.

Conflicts of Interest: The author declares that he has no known competing financial interests or personal relationships that could have appeared to influence the work reported in this paper.

References

1. Yeh, J.W.; Chen, S.K.; Lin, S.J.; Gan, J.Y.; Chin, T.S.; Shun, T.T.; Tsau, C.H.; Chang, S.Y. Nanostructured high-entropy alloys with multiple principal elements: Novel alloy design concepts and outcomes. *Adv. Eng. Mater.* **2004**, *6*, 299–303. [\[CrossRef\]](#)
2. Cantor, B.; Chang, I.T.H.; Knight, P.; Vincent, A.J.B. Microstructural development in equiatomic multicomponent alloys. *Mater. Sci. Eng. A* **2004**, *375–377*, 213–218. [\[CrossRef\]](#)
3. Chou, H.P.; Chang, Y.S.; Chen, S.K.; Yeh, J.W. Microstructure, thermophysical and electrical properties in $\text{Al}_x\text{CoCrFeNi}$ ($0 \leq x \leq 2$) high-entropy alloys. *Mater. Sci. Eng. B* **2009**, *163*, 184–189. [\[CrossRef\]](#)
4. Kao, Y.F.; Chen, S.K.; Chen, T.J.; Chu, P.C.; Yeh, J.W.; Lin, S.J. Electrical, magnetic, and Hall properties of $\text{Al}_x\text{CoCrFeNi}$ high-entropy alloys. *J. Alloys Compd.* **2011**, *509*, 1607–1614. [\[CrossRef\]](#)
5. Nagase, T.; Iijima, Y.; Matsugaki, A.; Ameyama, K.; Nakano, T. Design and fabrication of Ti–Zr–Hf–Cr–Mo and Ti–Zr–Hf–Co–Cr–Mo high-entropy alloys as metallic biomaterials. *Mater. Sci. Eng. C* **2020**, *107*, 110322. [\[CrossRef\]](#)
6. Liu, S.F.; Lin, W.T.; Zhao, Y.L.; Chen, D.; Yeli, G.; He, F.; Zhao, S.J.; Kai, J.J. Effect of silicon addition on the microstructures, mechanical properties and helium irradiation resistance of NiCoCr-based medium-entropy alloys. *J. Alloys Compd.* **2020**, *844*, 156162. [\[CrossRef\]](#)
7. Motallebzadeh, A.; Peighambaroust, N.S.; Sheikh, S.; Murakami, H.; Guo, S.; Canadinc, D. Microstructural, mechanical and electrochemical characterization of TiZrTaHfNb and $\text{Ti}_{1.5}\text{ZrTa}_{0.5}\text{Hf}_{0.5}\text{Nb}_{0.5}$ refractory high-entropy alloys for biomedical applications. *Intermetallics* **2019**, *113*, 106572. [\[CrossRef\]](#)
8. Edalati, P.; Floriano, R.; Tang, Y.; Mohammadi, A.; Pereira, K.D.; Luchessi, A.D.; Edalati, K. Ultrahigh hardness and biocompatibility of high-entropy alloy TiAlFeCoNi processed by high-pressure torsion. *Mater. Sci. Eng. C* **2020**, *112*, 110908. [\[CrossRef\]](#)
9. Sahlberg, M.; Karlsson, D.; Zlotea, C.; Jansson, U. Superior hydrogen storage in high entropy alloys. *Sci. Rep.* **2016**, *6*, 36770. [\[CrossRef\]](#) [\[PubMed\]](#)
10. Zhang, C.; Song, A.; Yuan, Y.; Wu, Y.; Zhang, P.; Lu, Z.; Song, X. Study on the hydrogen storage properties of a TiZrNbTa high entropy alloy. *Int. J. Hydrog. Energy* **2020**, *45*, 5367–5374. [\[CrossRef\]](#)
11. Cardoso, K.R.; Roche, V.; Jorge, A.M., Jr.; Antikeira, F.J.; Zepon, G.; Champion, Y. Hydrogen storage in MgAlTiFeNi high entropy alloy. *J. Alloys Compd.* **2021**, *858*, 158357. [\[CrossRef\]](#)
12. MacDonald, B.E.; Fu, Z.; Zheng, B.; Chen, W.; Lin, Y.; Chen, F.; Zhang, L.; Ivanisenko, J.; Zhou, Y.; Hahn, H.; et al. Recent progress in high entropy alloy research. *JOM* **2017**, *69*, 2024–2031. [\[CrossRef\]](#)
13. Pickering, E.J.; Jones, N.G. High-entropy alloys: A critical assessment of their founding principles and future prospects. *Int. Mater. Rev.* **2016**, *61*, 183–202. [\[CrossRef\]](#)
14. Li, D.Y.; Gao, M.C.; Hawk, J.A.; Zhang, Y. Annealing effect for the $\text{Al}_{0.3}\text{CoCrFeNi}$ high-entropy alloy fibers. *J. Alloys Compd.* **2019**, *778*, 23–29. [\[CrossRef\]](#)
15. Jiang, Z.F.; Chen, W.P.; Chu, C.L.; Fu, Z.Q.; Ivanisenko, J.; Wang, H.; Peng, S.Y.; Lu, Y.M.; Lavernia, E.J.; Hahn, H. Directly cast fibrous heterostructured $\text{FeNi}_{0.9}\text{Cr}_{0.5}\text{Al}_{0.4}$ high entropy alloy with low-cost and remarkable tensile properties. *Scr. Mater.* **2023**, *230*, 115421. [\[CrossRef\]](#)
16. Schonecker, S.; Li, X.J.; Wei, D.X.; Nozaki, S.; Kato, H.; Vitos, L.; Li, X.Q. Harnessing elastic anisotropy to achieve low-modulus refractory high-entropy alloys for biomedical applications. *Mater. Des.* **2022**, *215*, 110430. [\[CrossRef\]](#)
17. Zhang, T.; Shang, Z.; Chen, M.; He, J.; Lv, B.; Wang, X.; Xiong, X. High-Purity Nickel Prepared by Electron Beam Melting: Purification Mechanism. *Metall. Mater. Trans. B* **2014**, *45*, 164–174. [\[CrossRef\]](#)
18. Senkevich, K.S.; Serov, M.M.; Umarova, O.Z. Fabrication of intermetallic titanium alloy based on Ti_2AlNb by rapid quenching of melt. *Met. Sci. Heat Treat.* **2017**, *59*, 463–466. [\[CrossRef\]](#)
19. Vutova, K.; Stefanova, V.; Vassileva, V.; Atanasova-Vladimirova, S. Recycling of Technogenic CoCrMo Alloy by Electron Beam Melting. *Materials* **2022**, *15*, 4168. [\[CrossRef\]](#) [\[PubMed\]](#)

20. Zhang, G.; Ming, K.; Kang, J.; Huang, Q.; Zhang, Z.; Zheng, X.; Bi, X. High entropy alloy as a highly active and stable electrocatalyst for hydrogen evolution reaction. *Electrochim. Acta* **2018**, *279*, 19–23. [\[CrossRef\]](#)
21. Li, H.D.; Han, Y.; Zhao, H.; Qi, W.J.; Zhang, D.; Yu, Y.D.; Cai, W.W.; Li, S.X.; Lai, J.P.; Huang, B.L.; et al. Fast site-to-site electron transfer of high-entropy alloy nanocatalyst driving redox electrocatalysis. *Nat. Commun.* **2020**, *11*, 5437. [\[CrossRef\]](#)
22. Sarac, B.; Zadorozhnyy, V.; Berdonosova, E.A.; Ivanov, Y.P.; Klyamkin, S.; Gumrukcu, S.; Sarac, A.S.; Korol, A.; Semenov, D.; Zadorozhnyy, M.; et al. Hydrogen storage performance of the multi-principal-component CoFeMnTiVZr alloy in electrochemical and gas-solid reactions. *RSC Adv.* **2020**, *10*, 24613–24623. [\[CrossRef\]](#)
23. Zadorozhnyy, V.; Sarac, B.; Berdonosova, E.; Karazehir, T.; Lassnig, A.; Gammer, C.; Zadorozhnyy, M.; Ketov, S.; Klyamkin, S.; Eckert, J. Evaluation of hydrogen storage performance of ZrTiVNbCrFe in electrochemical and gas-solid reactions. *Int. J. Hydrog. Energy* **2020**, *45*, 5347–5355. [\[CrossRef\]](#)
24. Qiu, X.W. Corrosion behavior of Al₂CrFeCo_xCuNiTi high-entropy alloy coating in alkaline solution and salt solution. *Results Phys.* **2019**, *12*, 1737–1741. [\[CrossRef\]](#)
25. Löffler, T.; Waag, F.; Gökce, B.; Ludwig, A.; Barcikowski, S.; Schuhmann, W. Comparing the activity of complex solid solution electrocatalysts using inflection points of voltammetric activity curves as activity descriptors. *ACS Catal.* **2021**, *11*, 1014–1023. [\[CrossRef\]](#)
26. Nellaiappan, S.; Katiyar, N.K.; Kumar, R.; Parui, A.; Malviya, K.D.; Pradeep, K.G.; Singh, A.K.; Sharma, S.; Tiwary, C.S.; Biswas, K. High-Entropy alloys as catalysts for the CO₂ and CO reduction reactions: Experimental realization. *ACS Catal.* **2020**, *10*, 3658–3663. [\[CrossRef\]](#)
27. Mishra, R.K.; Sahay, P.P.; Shahi, R.R. Alloying, magnetic and corrosion behavior of AlCrFeMnNiTi high entropy alloy. *J. Mater. Sci.* **2019**, *54*, 4433–4443. [\[CrossRef\]](#)
28. Sarac, B.; Zadorozhnyy, V.; Ivanov, Y.P.; Spieckermann, F.; Klyamkin, S.; Berdonosova, E.; Serov, M.; Kaloshkin, S.; Greer, A.L.; Sarac, A.S.; et al. Transition metal-based high entropy alloy microfiber electrodes: Corrosion behavior and hydrogen activity. *Corros. Sci.* **2021**, *193*, 109880. [\[CrossRef\]](#)
29. Resnik, M.; Benčina, M.; Levičnik, E.; Rawat, N.; Iglič, A.; Junkar, I. Strategies for improving antimicrobial properties of stainless steel. *Materials* **2020**, *13*, 2944. [\[CrossRef\]](#)
30. Wang, S.P.; Xu, J. TiZrNbTaMo high-entropy alloy designed for orthopedic implants: As-cast microstructure and mechanical properties. *Mater. Sci. Eng. C* **2017**, *73*, 80–89. [\[CrossRef\]](#)
31. Cordeiro, J.M.; Nagay, B.E.; Ribeiro, A.L.R.; da Cruz, N.C.; Rangel, E.C.; Fais, L.M.G.; Vaz, L.G.; Barão, V.A.R. Functionalization of an experimental Ti-Nb-Zr-Ta alloy with a biomimetic coating produced by plasma electrolytic oxidation. *J. Alloys Compd.* **2019**, *770*, 1038–1048. [\[CrossRef\]](#)
32. Wang, R.; Tang, Y.; Li, S.; Zhang, H.; Ye, Y.; Zhu, L.; Ai, Y.; Bai, S. Novel metastable engineering in single-phase high-entropy alloy. *Mater. Des.* **2019**, *162*, 256–262. [\[CrossRef\]](#)
33. Wu, Y.Q.; Liaw, P.K.; Zhang, Y. Preparation of bulk TiZrNbMoV and NbTiAlTaV high-entropy alloys by powder sintering. *Metals* **2021**, *11*, 1748. [\[CrossRef\]](#)
34. Nutor, R.K.; Azeemullah, M.; Cao, Q.P.; Wang, X.D.; Zhang, D.X.; Jiang, J.Z. Microstructure and properties of a Co-free Fe₅₀Mn₂₇Ni₁₀Cr₁₃ high entropy alloy. *J. Alloys Compd.* **2021**, *851*, 156842. [\[CrossRef\]](#)
35. Wang, B.W.; Sun, M.; Li, B.B.; Zhang, L.J.; Lu, B.H. Anisotropic Response of CoCrFeMnNi High-Entropy Alloy Fabricated by Selective Laser Melting. *Materials* **2020**, *13*, 5687. [\[CrossRef\]](#)
36. Menghani, J.; Vyas, A.; More, S.; Paul, C.P.; Ingole, S. Preparation and Characterization of Laser Clad AlFeCuCrCoNi High-entropy Alloy (HEA) Coating for Improved Corrosion Performance. *Lasers Eng.* **2021**, *49*, 67–83.
37. Grandin, H.M.; Berner, S.; Dard, M. A review of titanium zirconium (TiZr) alloys for use in endosseous dental implants. *Materials* **2012**, *5*, 1348–1360. [\[CrossRef\]](#)
38. Sista, S.; Wen, C.; Hodgson, P.D.; Pande, G. The influence of surface energy of titanium-zirconium alloy on osteoblast cell functions in vitro. *J. Biomed. Mater. Res. Part A* **2011**, *97A*, 27–36. [\[CrossRef\]](#)
39. Al-Nawas, B.; Brägger, U.; Meijer, H.J.A.; Naert, I.; Persson, R.; Perucchi, A.; Quirynen, M.; Raghoobar, G.M.; Reichert, T.E.; Romeo, E.; et al. A double-blind randomized controlled trial (RCT) of Titanium-13Zirconium versus Titanium Grade IV small-diameter bone level implants in edentulous mandibles—Results from a 1-year observation period. *Clin. Implant. Dent. Relat. Res.* **2012**, *14*, 896–904. [\[CrossRef\]](#) [\[PubMed\]](#)
40. Gottlow, J.; Dard, M.; Kjellson, F.; Obrecht, M.; Sennerby, L. Evaluation of a new titanium-zirconium dental implant: A biomechanical and histological comparative study in the mini pig. *Clin. Implant. Dent. Relat. Res.* **2012**, *14*, 538–545. [\[CrossRef\]](#)
41. Xue, G.-L.; Yang, H.-L.; Xing, H.-X.; Ye, C.-R.; Liu, J.; Miao, J.-L.; Ruan, J.-M. Effect of Ti on microstructure, mechanical properties and corrosion resistance of Zr-Ta-Ti alloys processed by spark plasma sintering. *J. Cent. South Univ.* **2020**, *27*, 2185–2197. [\[CrossRef\]](#)
42. Bhola, S.M.; Bhola, R.; Mishra, B.; Olson, D.L. Electrochemical impedance spectroscopic characterization of the oxide film formed over low modulus Ti–35.5Nb–7.3Zr–5.7Ta alloy in phosphate buffer saline at various potentials. *J. Mater. Sci.* **2010**, *45*, 6179–6186. [\[CrossRef\]](#)
43. Sarac, B.; Sarac, A.S.; Eckert, J. Pd-based Metallic Glasses as Promising Materials for Hydrogen Energy Applications. *J. Electrochem. Soc.* **2023**, *170*, 014503. [\[CrossRef\]](#)

44. Sarac, B.; Zadorozhnyy, V.; Ivanov, Y.P.; Kvaratskheliya, A.; Ketov, S.; Karazehir, T.; Gumrukcu, S.; Berdonosova, E.; Zadorozhnyy, M.; Micusik, M.; et al. Surface-governed electrochemical hydrogenation in FeNi-based metallic glass. *J. Power Sources* **2020**, *475*, 228700. [CrossRef]
45. Sarac, B.; Karazehir, T.; Ivanov, Y.P.; Putz, B.; Greer, A.L.; Sarac, A.S.; Eckert, J. Effective electrocatalytic methanol oxidation of Pd-based metallic glass nanofilms. *Nanoscale* **2020**, *12*, 22586–22595. [CrossRef] [PubMed]
46. Mulder, W.H.; Sluyters, J.H.; Pajkossy, T.; Nyikos, L. Tafel current at fractal electrodes-Connection with admittance spectra. *J. Electroanal. Chem.* **1990**, *285*, 103–115. [CrossRef]
47. Gudić, S.; Vrsalović, L.; Kvrđić, D.; Nagode, A. Electrochemical behaviour of Ti and Ti-6Al-4V alloy in phosphate buffered saline solution. *Materials* **2021**, *14*, 7495. [CrossRef] [PubMed]
48. McCafferty, E. Validation of corrosion rates measured by the Tafel extrapolation method. *Corros. Sci.* **2005**, *47*, 3202–3215. [CrossRef]
49. Hwang, M.J.; Song, H.J.; Park, Y.J. Microstructure and Electrochemical Characterization of Ti-Sn Binary Alloys for Dental Applications. *Materials* **2022**, *15*, 6897. [CrossRef]
50. Wang, Z.; Yan, Y.; Wu, Y.; Huang, X.; Zhang, Y.; Su, Y.; Qiao, L. Corrosion and tribocorrosion behavior of equiatomic refractory medium entropy TiZr(Hf, Ta, Nb) alloys in chloride solutions. *Corros. Sci.* **2022**, *199*, 110166. [CrossRef]
51. Mietz, J.; Isecke, B. Monitoring of concrete structures with respect to rebar corrosion. *Constr. Build. Mater.* **1996**, *10*, 367–373. [CrossRef]
52. Zhou, Z.; Jiang, F.; Yang, F.; Yang, Y.; Liang, P. Novel laser cladding FeCoNiCrNb0.5Mox high-entropy alloy coatings with excellent corrosion resistance. *Mater. Lett.* **2023**, *335*, 133714. [CrossRef]
53. Shang, C.; Axinte, E.; Ge, W.; Zhang, Z.; Wang, Y. High-entropy alloy coatings with excellent mechanical, corrosion resistance and magnetic properties prepared by mechanical alloying and hot pressing sintering. *Surf. Interfaces* **2017**, *9*, 36–43. [CrossRef]
54. Wen, X.; Cui, X.; Jin, G.; Zhang, X.; Zhang, Y.; Zhang, D.; Fang, Y. Design and characterization of FeCrCoAlMn0.5Mo0.1 high-entropy alloy coating by ultrasonic assisted laser cladding. *J. Alloys Compd.* **2020**, *835*, 155449. [CrossRef]
55. Li, R.; Ren, J.; Zhang, G.-J.; He, J.-Y.; Lu, Y.-P.; Wang, T.-M.; Li, T.-J. Novel (CoFe₂NiV_{0.5}Mo_{0.2})_{100-x}Nb_x Eutectic High-Entropy Alloys with Excellent Combination of Mechanical and Corrosion Properties. *Acta Metall. Sin. (Engl. Lett.)* **2020**, *33*, 1046–1056. [CrossRef]
56. Shang, C.; Axinte, E.; Sun, J.; Li, X.; Li, P.; Du, J.; Qiao, P.; Wang, Y. CoCrFeNi(W_{1-x}Mo_x) high-entropy alloy coatings with excellent mechanical properties and corrosion resistance prepared by mechanical alloying and hot pressing sintering. *Mater. Des.* **2017**, *117*, 193–202. [CrossRef]
57. Wang, X.; Liu, Q.; Huang, Y.; Xie, L.; Xu, Q.; Zhao, T. Effect of Ti Content on the Microstructure and Corrosion Resistance of CoCrFeNiTi_x High Entropy Alloys Prepared by Laser Cladding. *Materials* **2020**, *13*, 2209. [CrossRef]
58. Liu, J.; Liu, H.; Chen, P.; Hao, J. Microstructural characterization and corrosion behaviour of AlCoCrFeNiTi_x high-entropy alloy coatings fabricated by laser cladding. *Surf. Coat. Technol.* **2019**, *361*, 63–74. [CrossRef]
59. Hu, S.; Li, T.; Li, X.; Zhang, G.; Li, J.; Guo, F.; Liu, D. Electrochemical behavior, passive film characterization and in vitro biocompatibility of Ti–Zr–Nb medium-entropy alloys. *J. Mater. Sci.* **2023**, *58*, 946–960. [CrossRef]
60. Wang, W.J.; Yang, K.H.; Wang, Q.T.; Dai, P.Q.; Fang, H.; Wu, F.J.; Guo, Q.H.; Liaw, P.K.; Hua, N.B. Novel Ti-Zr-Hf-Nb-Fe refractory high-entropy alloys for potential biomedical applications. *J. Alloy. Compd.* **2022**, *906*, 164383. [CrossRef]
61. Świąch, D.; Palumbo, G.; Piergies, N.; Pięta, E.; Szkudlarek, A.; Paluszkiewicz, C. Spectroscopic Investigations of 316L Stainless Steel under Simulated Inflammatory Conditions for Implant Applications: The Effect of Tryptophan as Corrosion Inhibitor/Hydrophobicity Marker. *Coatings* **2021**, *11*, 1097. [CrossRef]
62. Taylor, C.D.; Li, S.; Samin, A.J. Oxidation versus salt-film formation: Competitive adsorption on a series of metals from first-principles. *Electrochim. Acta* **2018**, *269*, 93–101. [CrossRef]
63. Loreto, S.; Cuyppers, B.; Brokken, J.; Van Doorslaer, S.; De Wael, K.; Meynen, V. The effect of the buffer solution on the adsorption and stability of horse heart myoglobin on commercial mesoporous titanium dioxide: A matter of the right choice. *Phys. Chem. Chem. Phys.* **2017**, *19*, 13503–13514. [CrossRef] [PubMed]
64. Da Cruz, R. Water Ionization Constant Study Guide. Available online: <https://www.inspiritvr.com/general-chemistry/acids-and-bases/water-ionization-constant-study-guide> (accessed on 5 May 2023).

Disclaimer/Publisher's Note: The statements, opinions and data contained in all publications are solely those of the individual author(s) and contributor(s) and not of MDPI and/or the editor(s). MDPI and/or the editor(s) disclaim responsibility for any injury to people or property resulting from any ideas, methods, instructions or products referred to in the content.